

---

**Conductance Simulations of Transport  
through a Quantum Dot in the Presence of a  
Sharp Drop in the Hybridization Function**

**Marc Ritter**

---

Bachelor Thesis  
Department of Physics, LMU München

supervised by  
Andreas Weichselbaum, PD Dr.



Munich, 2017



---

Simulation der Leitfähigkeit durch einen  
Quantenpunkt in der Gegenwart einen  
scharfen Abfalls in der  
Hybridisierungsfunktion

Marc Ritter

---

Bachelorarbeit  
Fakultät für Physik, LMU München

betreut von  
Andreas Weichselbaum, PD Dr.



München, 2017



### **Abstract**

A single-impurity Anderson model is used as a minimal model for a Quantum Point Contact (QPC), which is then solved with the Numerical Renormalization Group (NRG) method. As the coupling between the QPC and the surrounding conduction electron bath is strongly energy-dependent, sharp features occur in the hybridization function. Since we are interested in the regime at the band edge, where the hybridization is suppressed to zero, this necessitates the application of the recently developed Open Wilson Chain approach to the NRG. Overall this results in a minimal model that can be efficiently simulated at any temperature using NRG. The qualitative correspondence to experimental results is discussed for a range of possible parameter choices. The model reproduces the quantised step in conductance as a function of QPC gate voltage. At zero temperature, a sub-structure very similar to the 0.7 anomaly in transport through a QPC is found. At this stage, some qualitative differences to experimental observations occur at finite temperatures.



# Contents

<b>1</b>	<b>Introduction and Motivation</b>	<b>5</b>
<b>2</b>	<b>The Physical Model</b>	<b>7</b>
2.1	Single-Impurity Anderson Model (SIAM)	7
2.2	Resonant Level Model	8
2.3	Modelling a Quantum Point Contact Using a SIAM	9
2.3.1	Double-sided Fermi Function	9
2.3.2	Semicircle	10
2.3.3	Van Hove Ridges	10
2.4	Meir-Wingreen Formula	11
2.5	Friedel Sum Rule	12
2.6	Kondo Temperature	13
<b>3</b>	<b>Numerical Renormalization Group Method</b>	<b>14</b>
3.1	General Method	14
3.1.1	Discretization	14
3.1.2	Mapping to Wilson Chain	15
3.1.3	Iterative Diagonalization	16
3.2	Open Wilson Chains	17
<b>4</b>	<b>Analytic properties of the Non-Interacting SIAM</b>	<b>19</b>
4.1	Fixed Impurity Level Position	19
4.1.1	Spectral Function	19
4.1.2	Occupation Number	20
4.2	Shifted Impurity Level Position	22
<b>5</b>	<b>Results</b>	<b>24</b>
5.1	Parameter Choice	24
5.2	Cross-check between Analytic and NRG Results	24
5.3	Double-sided Fermi Function	24
5.4	Van Hove Ridges	27
5.5	Semicircle	29
5.6	Anomaly in the Conductance Step	30
5.7	Finite Temperature	32
<b>6</b>	<b>Conclusion and Outlook</b>	<b>33</b>
	<b>Appendix</b>	<b>35</b>
A	Kramers-Kronig Relations	35
B	Retarded Green's Functions	35
	<b>Bibliography</b>	<b>37</b>



# Chapter 1

## Introduction and Motivation

A *Quantum Point Contact* (QPC) is a very narrow constriction through which electrons move between two otherwise disconnected areas of an electron gas in effectively one-dimensional fashion. For instance, this constriction can be formed between two areas of a two-dimensional electron gas (2DEG) by two gates which generate an electric potential (see figure 1.1). In this setup, the width of the constriction can be modified by changing the gate voltage [2, 12, 18, 19].

Such a device has been realised in several experiments, where the conductance  $g$  through a QPC as a function of gate voltage was found to be quantised in steps of  $g_0 = \frac{2e^2}{h}$  [19]. Thomas et al. [18] unexpectedly discovered an additional structure at  $g \approx 0.7 g_0$ , which has become known as the *0.7 anomaly* [2]. Said structure forms a shoulder or a smaller step, the shape of which depends on a number of external parameters. In particular, dependence on temperature  $T$  and external magnetic field  $B$  have been extensively studied [1, 2, 18].

While a number of theoretical explanations have been proposed, the origin of the effect is still debated [1, 2, 12, 16]. Some explanations focus on observed similarities between the 0.7 anomaly and the Kondo effect, where the local moment of impurity states scatters conduction electrons at high temperatures while being screened at low temperatures leading to anomalous behaviour of the resistivity of certain dilute alloys [2, 11]. This motivated explanations on the basis of a quasi-localized state with local moment, for example by Meir et al. [16].

Assuming the existence of a quasi-localized state, a *single-impurity Anderson model* (SIAM) can be used as a minimal model for a QPC coupled to a 2DEG. This model is a considerable simplification, as the entire structure of the potential

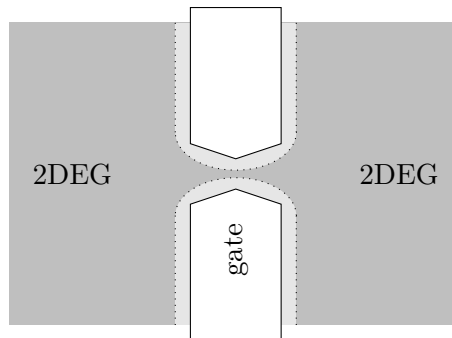


Figure 1.1: Schematic of a quantum point contact. Two gates (white) generate an electric potential (light grey) which forms a constriction to the movement of electrons in a lead connecting two areas of a 2-dimensional electron gas (dark grey).

---

landscape which forms the QPC is only represented by a single level with local on-site interaction and energy-dependent coupling strengths.

Solving the SIAM at low temperatures is non-trivial, as perturbation theory is not applicable in the low-temperature regime. This can be accomplished numerically using the *Numerical Renormalization Group* (NRG) method originally developed by Wilson [23] for the Kondo model [5, 14, 21]. However, the aforementioned model for the QPC is problematic for the standard approach: If the coupling between impurity level and bath modes contains weak contributions at finite energies, as is the case in the QPC model, certain significant contributions are neglected. Therefore, the recently developed *Open Wilson Chain* approach by Bruognolo et al. [3] will be employed.

The single-impurity Anderson model will be introduced in chapter 2, followed by an explanation of how the SIAM can be used as a minimal model for a QPC and the relations which will be used to calculate the conductance and occupation number. Chapter 3 contains a brief presentation of the Numerical Renormalization Group method and the Open Wilson Chain approach. Before these numerical methods are utilized, some analytical properties of the model are demonstrated in chapter 4. Numeric results calculated using NRG including qualitative comparisons to experimental results are shown in chapter 5. The final chapter 6 summarizes the results and mentions some starting points for future work.

## Chapter 2

# The Physical Model

### 2.1 Single-Impurity Anderson Model (SIAM)

The *single-impurity Anderson model* describes an impurity level coupled to a continuous non-interacting bath of states. Annihilation and creation operators of impurity states will be denoted  $d_\sigma$  and  $d_\sigma^\dagger$  respectively; annihilation and creation operators of bath states  $k$  will be denoted  $c_{k\sigma}$  and  $c_{k\sigma}^\dagger$ . As these operators describe spin- $\frac{1}{2}$ -fermions,  $\sigma$  only takes values  $\uparrow, \downarrow$ . These operators obey fermionic anticommutation relations, namely

$$\{d_\sigma^\dagger, d_{\sigma'}\} = \delta_{\sigma\sigma'} \quad \{c_{k\sigma}^\dagger, c_{k'\sigma'}\} = \delta_{\sigma\sigma'} \delta_{kk'} \quad (2.1)$$

The Hamiltonian, when expressed in terms of these operators, takes the form [5, 11, 21]

$$H = \underbrace{\sum_\sigma \epsilon_{d\sigma} d_\sigma^\dagger d_\sigma + U d_\uparrow^\dagger d_\uparrow d_\downarrow^\dagger d_\downarrow}_{\equiv H_{\text{imp}}} + \underbrace{\sum_{k\sigma} (V_{k\sigma} d_\sigma^\dagger c_{k\sigma} + V_{k\sigma}^* c_{k\sigma}^\dagger d_\sigma)}_{\equiv H_{\text{hyb}}} + \underbrace{\sum_{k\sigma} \epsilon_{k\sigma} c_{k\sigma}^\dagger c_{k\sigma}}_{\equiv H_{\text{bath}}} \quad (2.2)$$

$H$  consists of 3 parts:  $H_{\text{imp}}$  describes the energy  $\epsilon_{d\sigma}$  of the impurity state and the coulomb repulsion  $U$  of the two fermions in the double-occupation case,  $H_{\text{hyb}}$  describes the coupling  $V_{k\sigma}$  of the impurity to bath states, and  $H_{\text{bath}}$  accounts for the energy  $\epsilon_{k\sigma}$  of bath states. Typically, the energies and couplings are taken to be spin-independent.

The Hamiltonian can also be expressed in the energy representation as [5, 14]

$$H = H_{\text{imp}} + \sum_\sigma \int_{-1}^{+1} d\omega \sqrt{\frac{\Gamma(\omega)}{\pi}} (d_\sigma^\dagger c_{\omega\sigma} + c_{\omega\sigma}^\dagger d_\sigma) + \sum_\sigma \int_{-1}^{+1} d\omega \omega c_{\omega\sigma}^\dagger c_{\omega\sigma} \quad (2.3)$$

where

$$\Gamma(\omega) = \pi \sum_k |V_k|^2 \delta(\omega - \epsilon_k) \quad (2.4)$$

is called the *hybridization function*. It describes the hybridization of the impurity state with bath states at level  $\omega$ . Remarkably, it is the only information concerning the bath which is necessary to solve the single-impurity Anderson model. Using Kramers-Kronig relations (see appendix A), the full (complex) hybridization function  $\Delta(\omega)$  can be defined such that  $\Gamma(\omega) = -\text{Im} \Delta(\omega)$ : [11]

$$\Delta(\omega) = \sum_k \frac{|V_k|^2}{\omega^+ - \epsilon_k} \quad (2.5)$$

## 2.2 Resonant Level Model

The *resonant level model* (also known as non-interacting Anderson model) is a simplification to the SIAM, where the spin-up and spin-down impurity states are assumed to be non-interacting, i.e.  $U = 0$ . Thus, the spin-up and spin-down parts of the Hamiltonian decouple. Dropping the spin indices for simplicity, the Hamiltonian becomes [11]

$$H = \epsilon_d d^\dagger d + \sum_k \left( V_k d^\dagger c_k + V_k^* c_k^\dagger d \right) + \sum_k \epsilon_k c_k^\dagger c_k \quad (2.6)$$

Since the Hamiltonian is now quadratic, the choice of  $U = 0$  considerably simplifies the problem. In contrast to the full SIAM, analytic solutions based on the solution of the 1-particle problem can be derived in the non-interacting case, which can then be compared to the solutions obtained by numerical methods. The impurity spectral function  $A(\omega)$ , which gives the local density of states [11], can be determined by calculating the retarded Green's function  $G_{dd^\dagger}^R(\omega)$  (see appendix B). The starting point is the equation of motion<sup>1</sup> (B.4)

$$\omega^+ G_{dd^\dagger}^R = \overbrace{\langle \{d, d^\dagger\} \rangle}^1 + G_{[d,H],d^\dagger}^R = 1 + \epsilon_d G_{dd^\dagger}^R + \sum_k V_k G_{c_k d^\dagger}^R \quad (2.7)$$

Now, the Green's functions  $G_{c_k d^\dagger}^R$  can be calculated the same way:

$$\omega^+ G_{c_k d^\dagger}^R = \epsilon_k G_{c_k d^\dagger}^R + V_k^* G_{dd^\dagger}^R \quad (2.8)$$

$$\Rightarrow G_{dd^\dagger}^R(\omega) = \frac{1}{\omega^+ - \epsilon_d - \sum_k \frac{|V_k|^2}{\omega^+ - \epsilon_k}} = \frac{1}{\omega^+ - \epsilon_d - \Delta(\omega)} \quad (2.9)$$

The last term in the denominator of this expression is the full hybridization function from equation (2.5).

$$\Delta(\omega) = \sum_k \frac{|V_k|^2}{\omega^+ - \epsilon_k}$$

Equation (B.5) can be used to obtain the spectral function

$$A(\omega) = -\frac{1}{\pi} \text{Im} G_{dd^\dagger}^R(\omega) = \frac{\Gamma(\omega)/\pi}{(\omega - \epsilon_d - \text{Re} \Delta(\omega))^2 + (\Gamma(\omega))^2} \quad (2.10)$$

For a constant hybridization  $\Gamma(\omega) = \Gamma_0$ ,  $\text{Re} \Delta(\omega)$  vanishes and  $A(\omega)$  becomes a Lorentz peak centered on  $\epsilon_d$  of width  $\Gamma_0$ .

$$A(\omega) = \frac{\Gamma_0/\pi}{(\omega - \epsilon_d)^2 + \Gamma_0^2} \quad (2.11)$$

The spectral function is normalized to unity by construction, even for non-constant hybridization functions [6].

---

<sup>1</sup>The notation  $\omega^+$  is a shorthand for  $\omega + i\eta$ , where  $\eta > 0$ . It is used to obtain the Cauchy principal value by taking the limit  $\eta \rightarrow 0$  at the end of the calculation. Further details can be found in appendix A.

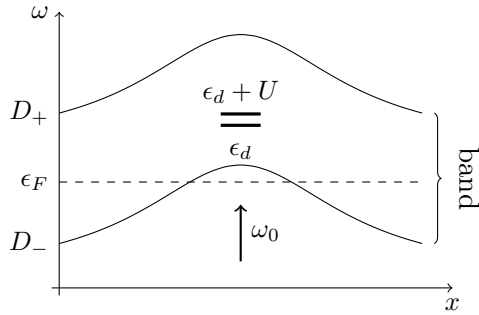


Figure 2.1: Approximation of a QPC with a single-impurity Anderson model. Even for a smooth potential, quasi-localised states exist. Thus, the QPC may be modelled as an impurity if a suitable hybridization function is used.

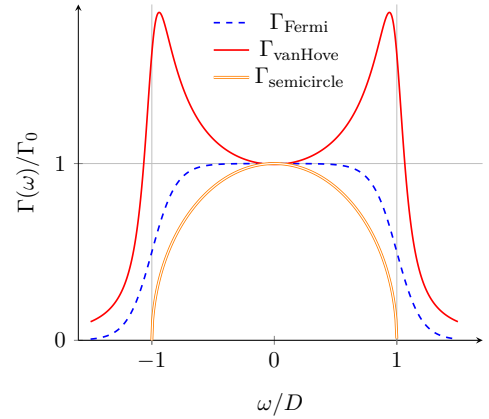


Figure 2.2: Hybridization functions for the QPC model from equations (2.12) and (2.19) using  $\delta = 0.1$  for both functions.

## 2.3 Modelling a Quantum Point Contact Using a SIAM

A minimal model for a quantum point contact may consist of the single level in a single-impurity Anderson model if the gate voltage introduces a potential barrier of similar magnitude to the Fermi energy  $\epsilon_F$ . The band is then bent upwards as shown in figure 2.1. As Meir, Hirose and Wingreen showed using spin-density functional theory [16], even a smooth potential barrier at the location of the QPC leads to a quasi-localised state, which will be considered the impurity state  $\epsilon_d$  of a SIAM. The coupling to band states corresponds to the hybridization in the SIAM. To model different gate voltages, the parameter  $\omega_0$  is used, which describes the band shift in respect to a symmetric configuration where the band edges are at  $\epsilon_F \pm D$ , with  $D$  being one-half of the bandwidth. The impurity level is then offset in parallel to the band edges, i.e.  $\epsilon_d = \epsilon_{d,0} + \omega_0$ .

As pointed out in section 2.2, the hybridisation function  $\Gamma$  is the only information about bath states which is necessary to solve the SIAM. There are several reasonable possibilities of choosing  $\Gamma$  which will be investigated in this thesis.

### 2.3.1 Double-sided Fermi Function

To model the conduction band, a double-sided Fermi function can be used. It is of the form

$$\Gamma_{\text{Fermi}}(\omega) = \Gamma_0 \left( f_\delta(\omega - D_-) - f_\delta(\omega - D_+) \right); \quad D_\pm = \omega_0 \pm D \quad (2.12)$$

where  $f_\delta(\omega) = 1 / (1 + \exp(\frac{\omega}{\delta}))$  is the Fermi function with sharpness  $\delta$ ,  $D$  is one-half of the bandwidth (such that for an unshifted band, the band edges are at  $\pm D$ ) and  $\Gamma_0$  is the parameter controlling the overall coupling strength. More precisely, it is the value of  $\Gamma_{\text{Fermi}}(\omega = 0)$  for an unshifted band  $\omega_0 = 0$ .<sup>2</sup>

<sup>2</sup>This is not exactly true, as the Fermi function  $f(\omega)$  only approaches 0 and 1 asymptotically as  $\omega \rightarrow +\infty$  and  $-\infty$  respectively. However, for  $\delta \ll D$ , the exponential decay is sufficiently fast such that the difference between  $\Gamma_0$  and  $\Gamma(0)$  is far below numerical accuracy. For example,  $|\Gamma_0 - \Gamma(0)| \approx 10^{-43} \Gamma_0$  for  $\delta/D = 10^{-2}$ .

---

### 2.3.2 Semicircle

In the region close to the QPC, transversal movement of the electrons is constrained to a very narrow channel, which can be reasonably approximated as a one-dimensional structure. The density of states of the first site of a semi-infinite tight-binding chain with equal couplings  $t$  and site energies  $\epsilon$  can be derived starting with its Green's function [11]

$$G(\omega) = \frac{1}{\omega^+ - \epsilon - \frac{t^2}{\omega^+ - \epsilon - \frac{t^2}{\omega^+ - \epsilon - \dots}}} = \frac{1}{\omega^+ - \epsilon - t^2 G(\omega)} \quad (2.13)$$

Multiplication with the denominator gives a quadratic equation for  $G(\omega)$ :

$$\underbrace{(\omega^+ - \epsilon)}_{\omega'} G(\omega) - t^2 G^2(\omega) - 1 = 0 \Rightarrow G(\omega) = \frac{1}{2t^2} \left( \omega' \pm \sqrt{\omega'^2 - 4t^2} \right) \quad (2.14)$$

The spectral function  $A(\omega)$  is obtained by taking the imaginary part of the negative square root (since  $A(\omega) > 0$ ):

$$A(\omega) = -\frac{1}{\pi} \text{Im} G(\omega) \propto \text{Im} \sqrt{\left(\frac{\omega'}{2t}\right)^2 - 1} = \begin{cases} \sqrt{1 - \left(\frac{\omega'}{2t}\right)^2} & \left|\frac{\omega'}{2t}\right| \leq 1 \\ 0 & \text{otherwise} \end{cases} \quad (2.15)$$

Clearly,  $A(\omega)$  describes a semicircle. However, in the vicinity of the QPC, the electric potential shifts the site energies upwards and  $\epsilon$  differs between sites. In that case, the density of states will be shifted upwards as well, while its shape remains largely the same. Below the lower band edge, however, the density of states is not perfectly zero due to contributions from lattice sites further away.

This behaviour was modelled using a shifted semicircle which is then broadened throughout with a Lorentzian to smoothen the band edge. Band shift is again controlled by the parameter  $\omega_0$ ,  $\Gamma_0$  controls the overall hybridization strength and  $D$  is the bandwidth. With these parameters,

$$\Gamma_{\text{semicircle}}(\omega) = \frac{\Gamma_0}{\mathcal{N}} \int_{-\infty}^{\infty} d\omega' \sqrt{1 - \left(\frac{\omega' - \omega_0}{D}\right)^2} \left( \frac{\delta/\pi}{(\omega - \omega')^2 + \delta^2} \right) \quad (2.16)$$

where  $\mathcal{N}$  is a normalization constant to allow  $\Gamma_0$  to be defined as  $\Gamma(\omega_0)$ .

### 2.3.3 Van Hove Ridges

As the QPC is coupled to quasi-one-dimensional leads on both sides, another reasonable hypothesis concerning the shape of the hybridisation function would be a proportionality to the density of states of an infinite (rather than a semi-infinite) chain. Its density of states can most easily be derived by observing that an infinite chain is a single site coupled to two identical semi-infinite chains with Green's functions  $G_l = G_r$ . Therefore, the Green's function is

$$\begin{aligned} G(\omega) &= \frac{1}{\omega^+ - \epsilon - t^2 G_l(\omega) - t^2 G_r(\omega)} = \frac{1}{\omega^+ - \epsilon - \left(\omega^+ - \epsilon - \sqrt{\omega'^2 - 4t^2}\right)} \\ &= \frac{1}{\sqrt{\omega'^2 - 4t^2}} \end{aligned} \quad (2.17)$$

---

from which the spectral function can be obtained by

$$A(\omega) = -\frac{1}{\pi} \text{Im} G(\omega) = \text{Im} \frac{-2t/\pi}{\sqrt{\left(\frac{\omega'}{2t}\right)^2 - 1}} = \begin{cases} \frac{2t/\pi}{\sqrt{1 - \left(\frac{\omega'}{2t}\right)^2}} & \left|\frac{\omega'}{2t}\right| \leq 1 \\ 0 & \text{otherwise} \end{cases} \quad (2.18)$$

This is the well-known density of states of a infinite tight-binding chain, where van Hove singularities proportional to  $1/\sqrt{1 - \omega^2}$  occur at the band edges. As in the case of a semi-infinite chain, adjusting the gate voltage simply offsets the spectral function by some  $\omega_0$ . Due to the varied potential landscape of the bath levels around the impurity, the system is not perfectly translationally invariant in 1D. This will smoothen singularities such that instead of divergences, smooth peaks (*van Hove ridges*) occur at the band edges. This reasoning is in part inspired by the local density of states in a QPC described by Bauer et al. [1].

In this thesis, the van Hove ridges were modelled by convolution of the van Hove singularities with a Lorentzian.

$$\Gamma_{\text{vanHove}}(\omega) = \frac{\Gamma_0}{\mathcal{N}} \int_{D_-}^{D_+} d\omega' \frac{1}{\sqrt{1 - \left(\frac{\omega' - \omega_0}{D}\right)^2}} \left( \frac{\delta/\pi}{(\omega - \omega')^2 + \delta^2} \right) \quad (2.19)$$

The meaning of  $D_{\pm}$  and  $\Gamma_0$  remains the same as above.  $\delta$  is again the parameter controlling sharpness, as it is the width of the Lorentz peak used to smoothen the van-Hove singularities, and  $\mathcal{N}$  is a normalization constant dependent on  $D$  and  $\delta$  to make sure  $\Gamma(\omega_0) = \Gamma_0$ .

A plot of the hybridization functions is shown in figure 2.2.

## 2.4 Meir-Wingreen Formula

For small voltages, where linear response theory is applicable, the conductance through a QPC can be obtained from the spectral function using the Meir-Wingreen formula for symmetric coupling: [17]

$$\frac{g}{g_0} = \int d\omega \pi \Gamma(\omega) A(\omega) \left( -\frac{\partial f(\omega)}{\partial \omega} \right) \quad (2.20)$$

where  $g_0 = \frac{2e^2}{h}$  is the conductance quantum of a spinful system and  $f$  is the Fermi function. This formula is very useful for NRG calculations, since the spectral function can be readily obtained using NRG. The derivative of the Fermi function is

$$-\frac{\partial f}{\partial \omega} = \frac{\beta/2}{1 + \cosh(\beta\omega)} \quad (2.21)$$

where  $\beta = 1/T$ . As the derivative of the Fermi function is 0 everywhere except around  $\omega = 0$ , the conductance is only dependent on the values of the spectral function and hybridization at small energies, which can be calculated very accurately using NRG. Furthermore, in contrast to the Kubo formula for linear conductance which is based on current operators, the Meir-Wingreen formula does not require any numerical derivatives that would introduce a major source of numerical errors.

---

## 2.5 Friedel Sum Rule

The Friedel sum rule is the explicit formulation of the intuitive observation that the change in electron density must be consistent with the number of electrons introduced by the impurity. The number of states introduced by the impurity which lie below the Fermi level  $\epsilon_F = 0$  must therefore be equal to the average occupation of the impurity level  $\langle n_d \rangle$  [6, 11].

$$\langle n_d \rangle = \int_{-\infty}^0 A(\omega) d\omega = -\frac{1}{\pi} \text{Im} \int_{-\infty}^0 \frac{d\omega}{\omega^+ - \epsilon_d - \Delta(\omega) - \Sigma(\omega)} \quad (2.22)$$

where the proper self-energy  $\Sigma(\omega)$  accounts for the interaction  $U$  [9, 11].

The integral can be rewritten using

$$\begin{aligned} \frac{\partial}{\partial \omega} \ln \left( \omega - \epsilon_d - \Delta(\omega) - \Sigma(\omega) \right) &= \frac{1 - \frac{\partial \Delta}{\partial \omega} - \frac{\partial \Sigma}{\partial \omega}}{\omega - \epsilon_d - \Delta(\omega) - \Sigma(\omega)} \\ &= \left( 1 - \frac{\partial \Delta}{\partial \omega} - \frac{\partial \Sigma}{\partial \omega} \right) G(\omega) \end{aligned} \quad (2.23)$$

The term  $\frac{\partial \Sigma}{\partial \omega} G(\omega)$  vanishes upon integration [11, 15]. The two remaining terms can be identified as the displaced charge of the bath in the presence of the impurity

$$\delta n_c = \int_{-\infty}^0 \frac{\partial \Delta / \partial \omega}{\omega^+ - \epsilon_d - \Delta(\omega) - \Sigma(\omega)} d\omega \quad (2.24)$$

and the scattering phase shift<sup>3</sup>  $\eta$  up to a factor of  $\pi$ : [11]

$$\eta = -\text{Im} \ln \left( \omega - \epsilon_d - \Delta(\omega) - \Sigma(\omega) \right) \Big|_{-\infty}^0 = -\tan^{-1} \left( \frac{b}{a} \right) \quad (2.25)$$

where, for convenience,  $a$  and  $b$  have been defined as the real and imaginary part of the argument to the logarithm, evaluated at 0:

$$a := -\epsilon_d - \text{Re} \Delta(0) - \text{Re} \Sigma(0) \quad (2.26)$$

$$b := -\text{Im} \Delta(0) - \text{Im} \Sigma(0) = \Gamma(0) \quad (2.27)$$

The last equality holds because  $\text{Im} \Sigma(0) = 0$ . [11, 15] As a first preliminary result,

$$\langle n_d \rangle + \delta n_c = \frac{\eta}{\pi} = -\frac{1}{\pi} \tan^{-1} \left( \frac{b}{a} \right) \quad (2.28)$$

The Green's function at  $\omega = 0$ , expressed in terms of  $a$  and  $b$ , is

$$G(0) = \frac{1}{(-\epsilon_d - \text{Re} \Delta(0) - \text{Re} \Sigma(0)) - i(\text{Im} \Delta(0) + \text{Im} \Sigma(0))} = \frac{a - ib}{a^2 + b^2} \quad (2.29)$$

Therefore, the spectral function at  $\omega = 0$  is

$$A(0) = \frac{b/\pi}{a^2 + b^2} = \frac{1}{\pi b} \frac{1}{1 + \cot^2 \eta} = \frac{1}{\pi b} \sin^2 \eta \quad (2.30)$$

---

<sup>3</sup>This derivation shows that for a wide band,  $\pi \langle n_d \rangle = \eta$ , the phase shift of a scattered particle at  $\omega = 0$ . This is true because  $G_{d\sigma, d\sigma}(\omega)$  is proportional to  $T$ , where  $T$  is the transmission matrix. As these relations are irrelevant for this thesis, they will not be discussed. For more details, see the derivation by Langreth [15] or pages 113–115 in the book by Hewson [11].

---

The value of the spectral function at  $\omega = 0$  and the occupation number are thus connected by [11]

$$(\pi\Gamma A)_{\omega=0} = \sin^2 \eta \approx \sin^2 (\pi \langle n_d \rangle) \quad (2.31)$$

for a wide, flat band ( $\frac{\partial \Delta}{\partial \omega} \approx 0$ ). This relation only holds approximately if the Fermi energy is near band edges, since there the displaced charge  $\delta n_c$  becomes significant.

In the limit  $T \rightarrow 0$ , the left side of (2.31) is equal to the conductance  $g/g_0$ , since the derivative of the Fermi function in the Meir-Wingreen formula (2.20) becomes a very sharp peak centered on the Fermi energy  $\epsilon_F = 0$  and thus [7]

$$\frac{g}{g_0} = \int d\omega \pi\Gamma(\omega) A(\omega) \left( -\frac{\partial f(\omega)}{\partial \omega} \right) = (\pi\Gamma A)_{\omega=0} \approx \sin^2 (\pi \langle n_d \rangle) \quad (2.32)$$

This relation will be used as a consistency check for the numeric method.

## 2.6 Kondo Temperature

In the particle-hole-symmetric case of  $\epsilon_d = -U/2$  and  $U, \Gamma \rightarrow \infty$  with  $U/\Gamma \gtrsim 10$  roughly constant, the SIAM transitions into a Kondo model for magnetic impurities [11]. In this context, the Kondo temperature is of interest, as it gives the order of magnitude of the dynamically generated lowest energy scale in the system. Consequently, it is the approximate temperature where significant deviations from the strongly-correlated and perturbatively not accessible zero-temperature regime arise. The Kondo temperature is intrinsically related to the spin dynamics since charge fluctuations are frozen out at much higher energy scales. Therefore, the Kondo temperature can be related to the inverse of the static spin susceptibility  $\chi_0$  by

$$T_K = \frac{1}{4\chi_0} \quad (2.33)$$

The static spin susceptibility is straightforwardly accessible within NRG. Further details (which are not important for the following) can be found in [5].

## Chapter 3

# Numerical Renormalization Group Method

### 3.1 General Method

The *Numerical Renormalization Group* (NRG) method is a numeric method for solving impurity problems at arbitrary temperature, in particular also below the Kondo temperature  $T_K$  where perturbation theory fails. This method uses a coarse-grained approximation to the continuous Hamiltonian where the Hamiltonian is discretized in a logarithmic scheme. The discrete Hamiltonian is then transformed to a semi-infinite chain. Because of the initially chosen logarithmic discretization, the energy scales of different chain sites are separated and the chain Hamiltonian can be solved iteratively using Wilson's method. The procedure will be briefly described, summarising the essential points of the work of Krishna-Murthy et al. [14] and the review by Bulla et al. [5]. As an example, the application of the NRG method on a SIAM will be presented.

#### 3.1.1 Discretization

The Hamiltonian can be written in energy representation as

$$H = H_{\text{imp}} + \sum_{\sigma} \int_{-1}^{+1} d\epsilon \sqrt{\frac{\Gamma(\epsilon)}{\pi}} (d_{\sigma}^{\dagger} c_{\epsilon\sigma} + c_{\epsilon\sigma}^{\dagger} d_{\sigma}) + \sum_{\sigma} \int_{-1}^{+1} d\epsilon \epsilon c_{\epsilon\sigma}^{\dagger} c_{\epsilon\sigma} \quad (3.1)$$

where  $\Gamma(\epsilon) = \pi\rho V_{\epsilon}^2$  and having chosen  $D := 1$  as the unit of energy. Now, the bath will be divided into several discretization intervals. To obtain energy scale separation, which becomes important in later steps, the discretization points must be chosen logarithmically as  $x_n = \Lambda^{-n}$  with dimensionless discretization parameter  $\Lambda > 1$  (typically  $\Lambda = 2$ ). For each interval, a complete set of orthonormal states can be constructed by Fourier expansion. The discrete approximation is then obtained by neglecting all but one state in each interval<sup>1</sup> and choosing appropriate coupling strengths. The discretization scheme is depicted in figure 3.1 (A). The bath Hamiltonian can be expressed in terms of the fundamental frequency state annihilation / creation operators  $a_{n\sigma} / a_{n\sigma}^{\dagger}$  for positive and  $b_{n\sigma} / b_{n\sigma}^{\dagger}$  for negative frequency, where positive (negative) energies correspond to particles above (within) the Fermi sea, respectively.

$$H_{\text{bath}} = \frac{1}{2} (1 + \Lambda^{-1}) \sum_{n=0}^{\infty} \Lambda^{-n} (a_{n\sigma}^{\dagger} a_{n\sigma} - b_{n\sigma}^{\dagger} b_{n\sigma}) \quad (3.2)$$

---

<sup>1</sup>Only the state related to the fundamental Fourier frequency  $\omega_n$  in each interval is kept.

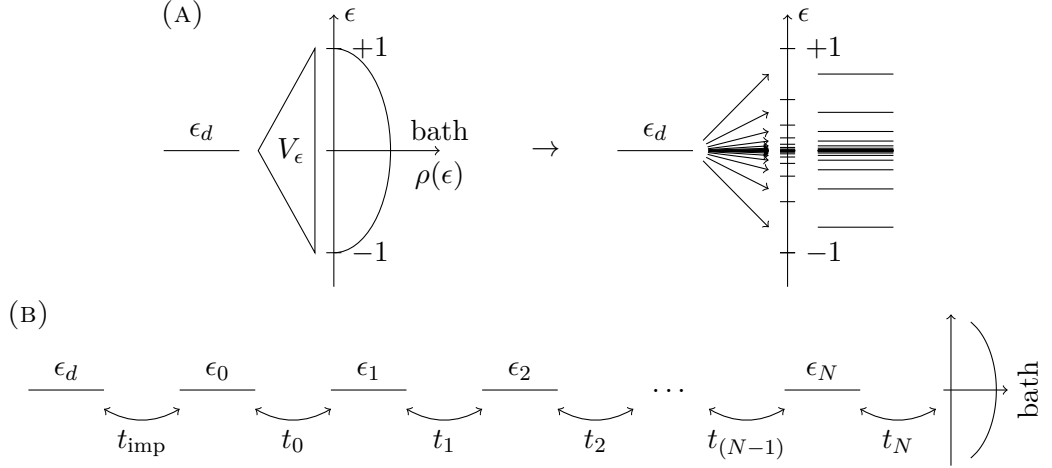


Figure 3.1: Mapping of the Hamiltonian from the energy representation to a Wilson chain. (A) Transition from the continuous to discretized bath. (B) Wilson chain of length  $N$  with site energies  $\epsilon_i$  and couplings  $t_i$ .

To reduce artefacts which occur due to the specific position of the discretization points, a method proposed by Oliveira et al. [10, 24] will be used. Instead of choosing  $x_n = \Lambda^{-n}$ , the discretization scheme is modified such that  $x_{n=0} = 1$ ;  $x_{n \geq 1} = \Lambda^{-(n+z)}$ , introducing a parameter  $0 \leq z < 1$ . Then, after calculating quantities for different values of  $z$ , the uniform average of these results over  $z \in [0, 1[$  mitigates discretization artefacts to a large extent. This method is also known as “ $z$ -averaging”.

### 3.1.2 Mapping to Wilson Chain

By introducing a new *local* operator

$$f_{0\sigma} = \frac{1}{\sqrt{2}} \int_{-1}^{+1} dk a_{k\sigma} = \sqrt{\frac{1 + \Lambda^{-1}}{2}} \sum_{n=0}^{\infty} \Lambda^{-n/2} (a_{n\sigma} + b_{n\sigma}) \quad (3.3)$$

the hybridization part of the Hamiltonian can be expressed in a simple form:

$$H_{\text{hyb}} = \sqrt{\frac{2\Gamma}{\pi}} \left( d_{\sigma}^{\dagger} f_{0\sigma} + f_{0\sigma}^{\dagger} d_{\sigma} \right) \quad (3.4)$$

where the prefactor of  $\sqrt{2}$  comes from the integrated hybridization function for a box distribution of width  $2D = 2$ . As  $a_{n\sigma}$  and  $b_{n\sigma}$  are not orthogonal to  $f_{0\sigma}$ , the Hamiltonian needs to be expressed in a new orthonormal basis containing  $f_{0\sigma}$ . A suitable transformation can be found by using the *Lanczos algorithm*, which is a standard algorithm that takes a hermitian matrix and constructs a unitary transformation to a basis in which the input matrix is tridiagonal [8, 11]. This algorithm is initialized with an arbitrary start vector which will become the first vector in the basis set. Thus, by choosing  $f_{0\sigma}$  as the start vector, the algorithm can be used to construct a basis  $\{f_{n\sigma}\}$  which contains  $f_{0\sigma}$  and in which  $H_{\text{bath}}$  is tridiagonal:

$$H = H_{\text{imp}} + \sqrt{\frac{2\Gamma}{\pi}} \left( d_{\sigma}^{\dagger} f_{0\sigma} + f_{0\sigma}^{\dagger} d_{\sigma} \right) + \sum_{n=0}^{\infty} \left( \epsilon_n f_{n\sigma}^{\dagger} f_{n\sigma} + t_n f_{n\sigma}^{\dagger} f_{(n+1)\sigma} + t_n f_{(n+1)\sigma}^{\dagger} f_{n\sigma} \right) \quad (3.5)$$

---

If a logarithmic discretization scheme has been chosen, the couplings  $t_n$  fall off exponentially (proportional to  $\Lambda^{-n/2}$ ), leading to energy scale separation of different contributions to the Hamiltonian. This allows the chain Hamiltonian to be iteratively solved using Wilson's NRG method [5].

### 3.1.3 Iterative Diagonalization

The tridiagonal Hamiltonian (3.5) can be expressed as the limit

$$H = \lim_{N \rightarrow \infty} \Lambda^{-\frac{1}{2}(N-1)} H_N \quad (3.6)$$

of a series of Hamiltonians

$$H_N = \Lambda^{\frac{1}{2}(N-1)} \left( H_{\text{imp}} + \sqrt{\frac{2\Gamma}{\pi}} (d_{\sigma}^{\dagger} f_{0\sigma} + f_{0\sigma}^{\dagger} d_{\sigma}) + \sum_{n=0}^N \epsilon_n f_{n\sigma}^{\dagger} f_{n\sigma} + \sum_{n=0}^{N-1} t_n (f_{n\sigma}^{\dagger} f_{(n+1)\sigma} + f_{(n+1)\sigma}^{\dagger} f_{n\sigma}) \right) \quad (3.7)$$

where the factors  $\Lambda^{\pm\frac{1}{2}(N-1)}$  cancel the  $N$ -dependence of  $t_{N-1}$  such that the lowest energy contribution is always of order 1. The relation between two successive Hamiltonians is given by

$$H_{N+1} = \sqrt{\Lambda} H_N + \Lambda^{N/2} \left( \epsilon_{(N+1)} f_{(N+1)\sigma}^{\dagger} f_{(N+1)\sigma} + t_N f_{N\sigma}^{\dagger} f_{(N+1)\sigma} + t_N f_{(N+1)\sigma}^{\dagger} f_{N\sigma} \right) \quad (3.8)$$

where

$$H_0 = \Lambda^{-1/2} \left( H_{\text{imp}} + \epsilon_0 f_{0\sigma}^{\dagger} f_{0\sigma} + \sqrt{\frac{2\Gamma}{\pi}} (d_{\sigma}^{\dagger} f_{0\sigma} + f_{0\sigma}^{\dagger} d_{\sigma}) \right) \quad (3.9)$$

Now, the actual computation will be performed iteratively. Provided the Hamiltonian  $H_N$  has already been diagonalized, the step  $H_N \rightarrow H_{N+1}$  corresponds to adding a new site to the chain. The eigenbasis of  $H_{N+1}$  can be constructed from the known eigenstates of  $H_N$  and basis states of the new site  $N+1$  [5].

This iterative method leads to an exponentially growing number of states. Keeping all states in memory and performing numerical diagonalization of exponentially growing matrices is computationally too expensive. However, since NRG calculations are mainly concerned with low-energy properties of the system, states that do not contribute to low-energy behaviour can simply be discarded. It is at this point where energy scale separation becomes important: As the contribution of the  $N$ th site falls off exponentially with  $N$ , one can in practice assume that high-energy states have exponentially negligible contribution to low-energy states of future iterations. Thus, at every iteration step, states with energies greater than a fixed energy<sup>2</sup>  $E_{\text{trunc}}$  are discarded [5, 14, 21, 22].

The convergence of NRG is exponential in the number of kept states for given  $\Lambda$ . In practice, convergence has to be checked. More detailed discussions of the truncation scheme, which shall not be presented here, can be found in the review by Bulla et al. [5], and a method for a quantitative estimation of the inaccuracy due to the discarded states is presented by Weichselbaum in [20].

---

<sup>2</sup>Alternatively, only a fixed number  $N_{\text{states}}$  of states with the lowest energies are kept and all states with higher energies are discarded.

## 3.2 Open Wilson Chains

The model for a QPC described in section 2.3 is problematic for the standard NRG method due to the shape of the hybridization functions  $\Gamma(\omega)$ , which contain very weakly coupled levels at finite energies. This results in non-monotonous behaviour of the couplings between sites in the Wilson chain. At some late iteration, a strong coupling  $t_n$  will occur, violating energy scale separation. This problem can be solved using the *Open Wilson Chain* approach by calculating the energies  $\epsilon_n$  and couplings  $t_n$  on the level of Green's functions [3].

Postulating that the bath correlator  $G^{\text{bath}} \equiv G_0$  can be expressed as the coupling to a single site which is in turn coupled to a new bath, the bath correlator can be expressed in the same form as the resonant level Green's function:

$$G_0(\omega) = \frac{1}{\omega^+ - \epsilon_0 - \Sigma_0(\omega)} \quad (3.10)$$

where  $\epsilon_0$  is the level energy and  $\Sigma_0$  the hybridisation energy. Now, the level energy  $\epsilon_0$  is equal to the expectation value of  $\omega$ :

$$\epsilon_0 = \int d\omega \omega A_0(\omega) = -\frac{1}{\pi} \int d\omega \omega \text{Im} G_0(\omega) \quad (3.11)$$

A derivation of this fact and further details can be found in [3]. The hybridisation energy can then be obtained by inverting equation (3.10):  $\Sigma_0(\omega) = \omega - \epsilon_0 - 1/G_0(\omega)$

$\Sigma_0$  can be subdivided into two parts, the coupling to the *slow* (low-energy) and *fast* (high-energy) bath. Quantities related to the slow and fast baths will be referred to with an index  $S$  or  $F$ , respectively. This subdivision is performed by weight functions  $w^S(\omega)$  and  $w^F(\omega)$  on the imaginary part of the hybridization [3]. Here, Heaviside  $\theta$  functions were used<sup>3</sup> as weight functions  $w^{S,F}(\omega) = \theta(\pm(\omega - \omega_{\text{trunc}}))$ :

$$\text{Im} \Sigma_0^{S,F}(\omega) = \theta(\pm(\omega - \omega_{\text{trunc}})) \text{Im} \Sigma_0(\omega); \quad \Sigma_0(\omega) = \Sigma_0^F(\omega) + \Sigma_0^S(\omega) \quad (3.12)$$

The full hybridisation energies can then be obtained using the well-known Kramers-Kronig relations (see appendix A).

As it was previously postulated that  $\Sigma_0^S$  represents the full (i.e. complex) hybridization function of a new bath  $S_0$ , the above procedure can be iteratively applied to the slow hybridization functions  $\Sigma_i^S$  using  $\Sigma_i^F = G_{i+1}$ . Thus, an exact continued fraction expansion of  $G^{\text{bath}}$  can be obtained [3].

$$G^{\text{bath}} = \frac{1}{\omega - \epsilon_0 - \Sigma_0^F - \frac{|t_0^S|^2}{\omega - \epsilon_1 - \Sigma_1^F - \frac{|t_1^S|^2}{\dots - \frac{|t_{N-1}^S|^2}{\omega - \epsilon_N - \Sigma_N^F - \Sigma_N^S}}} \quad (3.13)$$

The remaining hybridisation energies  $\Sigma_{1\dots N}^F$  and  $\Sigma_N^S$  are then absorbed into the level energies  $\epsilon$  by

$$\epsilon_i \rightarrow \epsilon_i + \text{Re} \Sigma_i^F(0) \quad (i \neq N); \quad \epsilon_N \rightarrow \epsilon_N + \text{Re} \Sigma_N^F(0) + \text{Re} \Sigma_N^S(0) \quad (3.14)$$

as this is equivalent to an approximation using second order perturbation theory:

$$\text{Re} \Sigma_i^F(0) = \frac{1}{\pi} \int d\omega \frac{\text{Im} \Sigma_i^F(\omega)}{\omega} = - \int d\omega \frac{\Gamma_i^F(\omega)}{\omega} \quad (3.15)$$

<sup>3</sup>Instead of using Heaviside  $\theta$  functions to truncate, weight functions  $w^{S,F}(\omega)$  (e.g. logistic functions) can be chosen such that  $w^S(\omega) + w^F(\omega) = 1$  to truncate more smoothly. For the model considered in this thesis, Heaviside  $\theta$  functions will suffice.

---

In addition, this approximation reproduces  $\text{Re} \Sigma^{\text{bath}}(0)$  correctly. For a symmetric hybridisation  $\Gamma(\omega)$ ,  $\text{Re} \Sigma$  vanishes. Corrections to  $\epsilon$  are therefore only relevant for asymmetric hybridisation functions, as is the case in this thesis [3].

The corrected site energies and couplings can then be used in an NRG run akin to the standard NRG method by constructing what Bruognolo et al. [3] refer to as a *renormalized Wilson chain*. Since corrections to the site energies caused by fast baths are now included in the Hamiltonian, an NRG run using a renormalized Wilson chain remains accurate even for very asymmetric hybridization functions.

## Chapter 4

# Analytic properties of the Non-Interacting SIAM

### 4.1 Fixed Impurity Level Position

As a first step, the non-interacting ( $U = 0$ ) single-impurity Anderson model (resonant level model) will be considered. Because it can be solved analytically, some properties of the full SIAM can be understood more easily in this simplified version. It is also useful as a consistency check for the numeric method.

To understand the behaviour of the non-interacting SIAM in the case of asymmetric hybridization, particularly near band edges, only the band will be shifted in this first section. The impurity level stays at  $\epsilon_d = 0 = \epsilon_F$  and, since some features of the resonant level model are more easily understood in this regime, a small overall hybridization of  $\Gamma_0 = 0.01$  was chosen.

#### 4.1.1 Spectral Function

In section 2.2, the spectral function for the resonant level model was derived. It is given by equation (2.10)

$$A(\omega) = \frac{\Gamma(\omega)/\pi}{(\omega - \epsilon_d - \text{Re } \Delta(\omega))^2 + (\Gamma(\omega))^2}$$

where  $\Gamma(\omega) = -\text{Im } \Delta(\omega)$  is the hybridisation function, and  $\text{Re } \Delta(\omega)$  can be obtained from  $\Gamma(\omega)$  using Kramers-Kronig relations (see appendix A). Figure 4.1 contains plots of spectral functions for different values of  $\omega_0$ .

In the symmetric case  $\omega_0 = 0$ ,  $\text{Re } \Delta(\omega)$  is small for  $\omega \approx 0$  (see figure 4.2). For small  $\omega$ , the spectral function is therefore very similar to a Lorentz peak with width  $\Gamma$ , which is the spectral function in the case of constant  $\Gamma(\omega) = \Gamma$ . Because the Meir-Wingreen formula (2.20)

$$\frac{g}{g_0} = \int d\omega \pi \Gamma(\omega) A(\omega) \left( -\frac{\partial f(\omega)}{\partial \omega} \right)$$

only samples the spectral function in the vicinity of the Fermi energy  $\epsilon_F = 0$ , the conductance for a symmetric double-sided Fermi function with sufficient bandwidth is very close to  $g/g_0 = 1$ .

For values  $\omega_0 \neq 0$ ,  $\text{Re } \Delta(\omega)$  is shifted the same way as  $\Gamma(\omega)$ . In the non-symmetric case,  $\text{Re } \Delta(0) \neq 0$ : the peak of the spectral function is displaced with respect to  $\epsilon_d$  by  $\text{Re } \Delta(0)$ . Thus, the maximum of the spectral function is shifted away from the Fermi

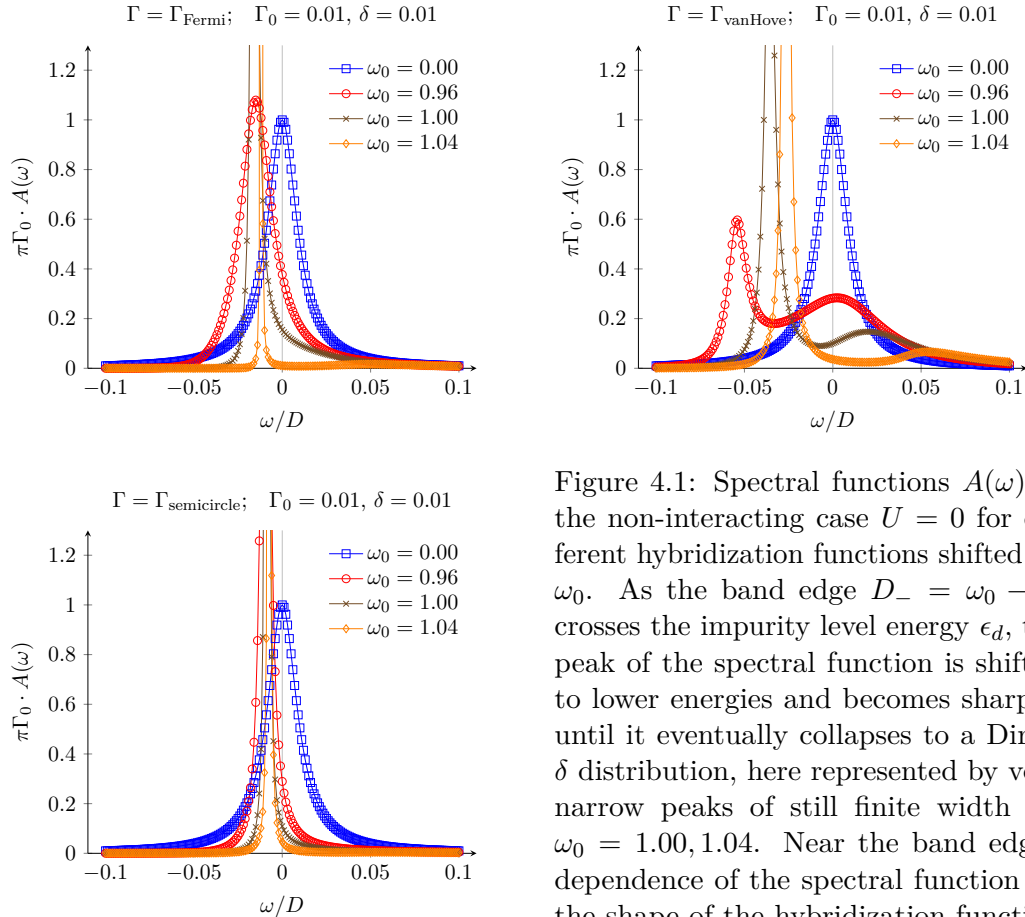


Figure 4.1: Spectral functions  $A(\omega)$  in the non-interacting case  $U = 0$  for different hybridization functions shifted by  $\omega_0$ . As the band edge  $D_- = \omega_0 - D$  crosses the impurity level energy  $\epsilon_d$ , the peak of the spectral function is shifted to lower energies and becomes sharper, until it eventually collapses to a Dirac- $\delta$  distribution, here represented by very narrow peaks of still finite width for  $\omega_0 = 1.00, 1.04$ . Near the band edges, dependence of the spectral function on the shape of the hybridization function is clearly visible.

energy and the conductance drops significantly already for  $|\omega_0| < D$ . Figure 4.2 shows the behaviour of the conductance  $g/g_0$  as a function of  $\omega_0$ .

For large values of  $|\omega_0| > D$ , the hybridisation is very weak and the system resembles an uncoupled single level. Therefore, the spectral function approaches a Dirac- $\delta$  distribution, the peak of which is displaced with respect to  $\epsilon_d$  by  $\text{Re } \Delta(\omega)$ .

#### 4.1.2 Occupation Number

To verify the Friedel sum rule (2.31), the average occupation number  $\langle n_d \rangle$  has been calculated for  $T = 0$  by integrating the spectral function over energies below the Fermi edge (see figure 4.3). As expected, the relation  $g/g_0 = \sin^2(\pi \langle n_d \rangle)$  from equation (2.32) holds everywhere except near the band edges.

In the symmetric case  $\omega_0 = 0$ , the spectral function is symmetric as well; therefore,  $\langle n_d \rangle$  is exactly  $\frac{1}{2}$ . In the case of a double-sided Fermi hybridization function, the impurity level is progressively shifted to lower energies as the band is shifted upwards. Thus, occupation number grows smoothly. At the band edge, a sudden (but smooth) transition occurs, where the spectral function becomes sharper and approaches the  $\delta$  distribution. Only a very small portion of its weight remains at energies within the band. Shifting the band even further results in very weak hybridisation. While the value of  $\text{Re } \Delta(0)$  shrinks as  $\omega_0$  grows further, this small shift is sufficient to place the entire weight of the peak in the spectral function below the Fermi edge, as it now resembles a  $\delta$  distribution. Consequently, having  $\epsilon_d = 0$ , the impurity level is nearly always occupied ( $\langle n_d \rangle \approx 1$ ) for  $\omega_0 > D$ .

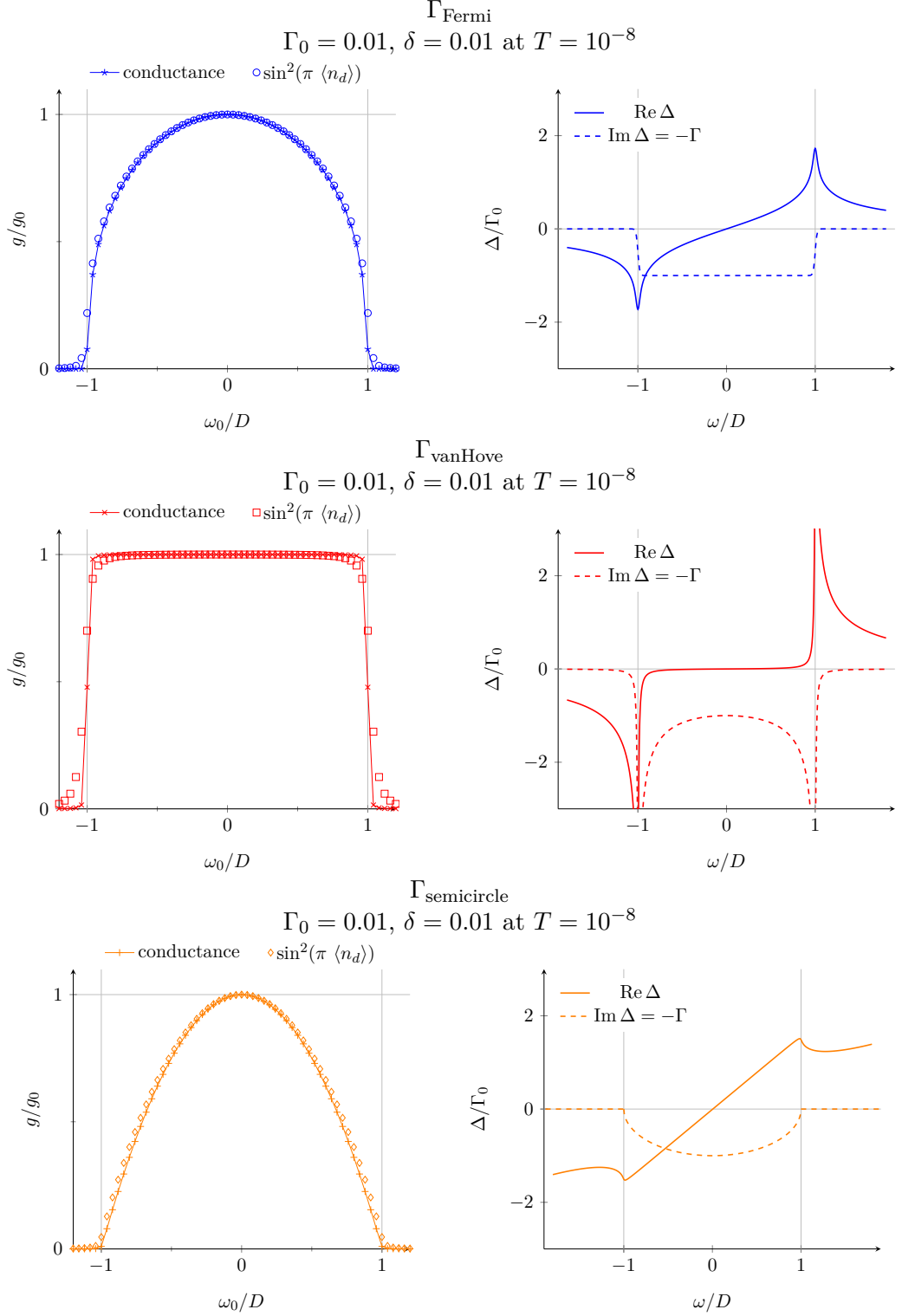


Figure 4.2: Conductance through the QPC as a function of band shift  $\omega_0$  (left column) and real and imaginary part of the spectral function (right column). Additionally,  $\sin^2(\pi \langle n_d \rangle)$  has been overlaid to verify the Friedel sum rule (2.31). The dependence of  $g/g_0$  on the real part of the spectral function is clearly visible. The difference between the conductance values and  $\sin^2(\pi \langle n_d \rangle)$  near band edges is due to the neglected displacement of bath charges. The same parameters as in figure 4.1 were used.

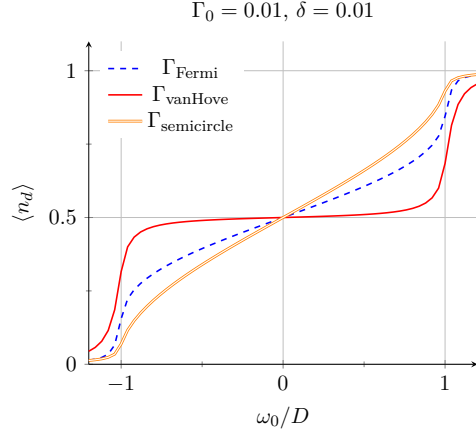


Figure 4.3: Expectation value of the impurity occupation number as a function of band shift  $\omega_0$ . The same parameters as in figure 4.1 were used.

For negative values of  $\omega_0$ , the behaviour of the spectral function is simply mirrored at the Fermi edge. Therefore, the conductance  $g/g_0$  is the same for  $\pm\omega_0$  and the occupation number is mirrored such that  $\langle n_d \rangle(-\omega_0) = 1/2 - \langle n_d \rangle(+\omega_0)$ .

## 4.2 Shifted Impurity Level Position

This section will discuss the behaviour of the non-interacting SIAM at similar parameters to those that will be used to model the QPC. In the model, the impurity level is shifted together with the hybridization function:  $\epsilon_d = \omega_0 - U/2$ . Since a quantum point contact is intrinsically open to the bath, large values of the overall hybridization  $\Gamma_0 = 0.5$  are assumed.

In the non-interacting case, the behaviour is quite simple, since the impurity level is shifted together with  $\omega_0$ . Therefore, the spectral function is shifted the same way as the rest of the system while its shape remains unchanged, as shown in figure 4.5. This implies that the conductance curves for different values of  $\omega_0$  (see figure 4.4) are a mirrored image of the spectral function multiplied with  $\Gamma(\omega)$ . In the case of  $\Gamma_{\text{vanHove}}$ , the peaks of  $A$  and  $\Gamma_{\text{vanHove}}$  combine to form a single peak in the conductance.

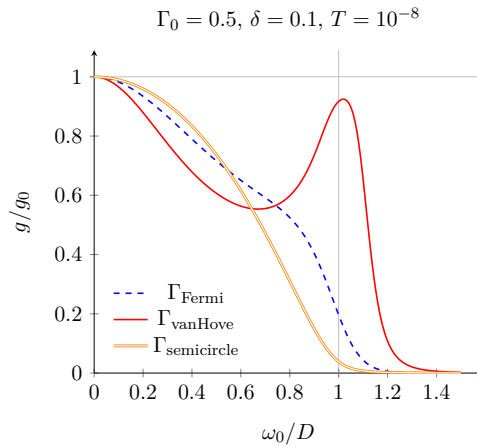


Figure 4.4: Conductances for different hybridization functions in the non-interacting case obtained using analytic methods.

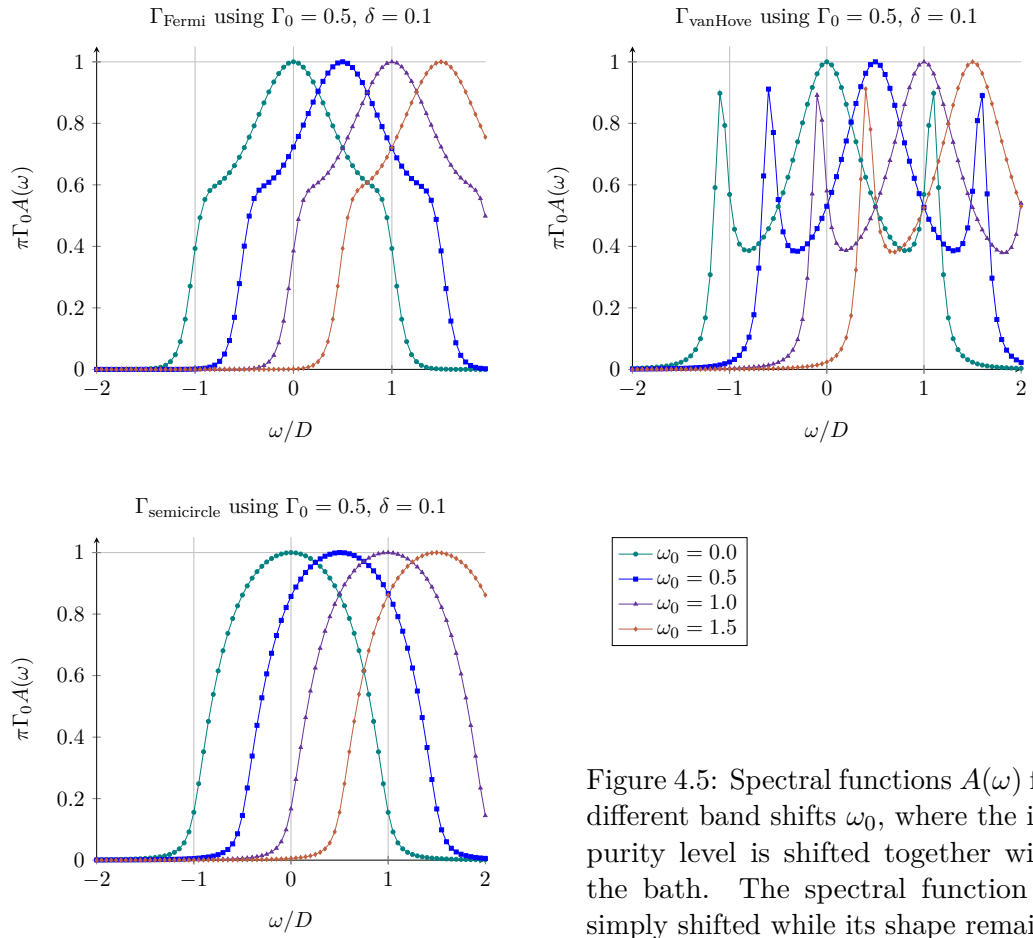


Figure 4.5: Spectral functions  $A(\omega)$  for different band shifts  $\omega_0$ , where the impurity level is shifted together with the bath. The spectral function is simply shifted while its shape remains unchanged.

# Chapter 5

## Results

### 5.1 Parameter Choice

Results for  $U > 0$  were obtained using Open Wilson Chain approach to the NRG. In the first part of this chapter, calculations were performed for a very low temperature of  $T = 10^{-8}$ . Since this value is below all energy scales in this problem including the Kondo temperature  $T_K$ , this choice corresponds to the zero-temperature case. Finite-temperature results are given in the last section of this chapter.

As already mentioned, a quantum point contact is intrinsically open towards the baths and cannot be described as an isolated quantum dot. Therefore, a value of  $\Gamma_0 = 0.5$  has been chosen to reflect the expectation of a total coupling strength on the order of bandwidth  $D = 1$ . To get a general idea of the behaviour of the conductance for different hybridization functions, a somewhat larger value  $\delta = 0.1$  was chosen, given that one would expect smooth transitions also in the experiment. Besides, this also avoids any problems with numerical inaccuracy by initially using very smooth hybridization functions. However, some features are only visible for small values of  $\delta$  that will be explored after finding parameter ranges for which the overall behaviour of the conductance is consistent with the experimentally observed step from  $g = 0$  to  $g = g_0$ .

### 5.2 Cross-check between Analytic and NRG Results

As a cross-check, analytic and numeric results for  $U = 0$  using the same parameters have been compared. The conductance for different hybridization functions is shown in figures 5.1, 5.6 and 5.7, where the on-site interaction strength was varied from no interaction ( $U = 0$ ) to interaction strengths on the order of the hybridization ( $U = 0.5$ ). Analytic results for the non-interacting case are shown as well. The analytic and NRG results match closely, confirming the previous assertion that the NRG method together with the Meir-Wingreen formula is able to obtain conductances with high accuracy.

### 5.3 Double-sided Fermi Function

In the case of  $\Gamma = \Gamma_{\text{Fermi}}$ , the spectral function for low interaction strengths is similar to a Lorentz peak with suppressed tails. Since the hybridization is on the same order of magnitude as the bandwidth, the spectral function is as wide as the entire band. The conductance for  $\omega_0 > D$ , i.e. a band which has been shifted above the Fermi edge in its entirety, is suppressed by vanishing  $\Gamma(\omega)$ . This effect accounts for the shoulder visible in figure 5.1. It occurs most prominently in the non-interacting

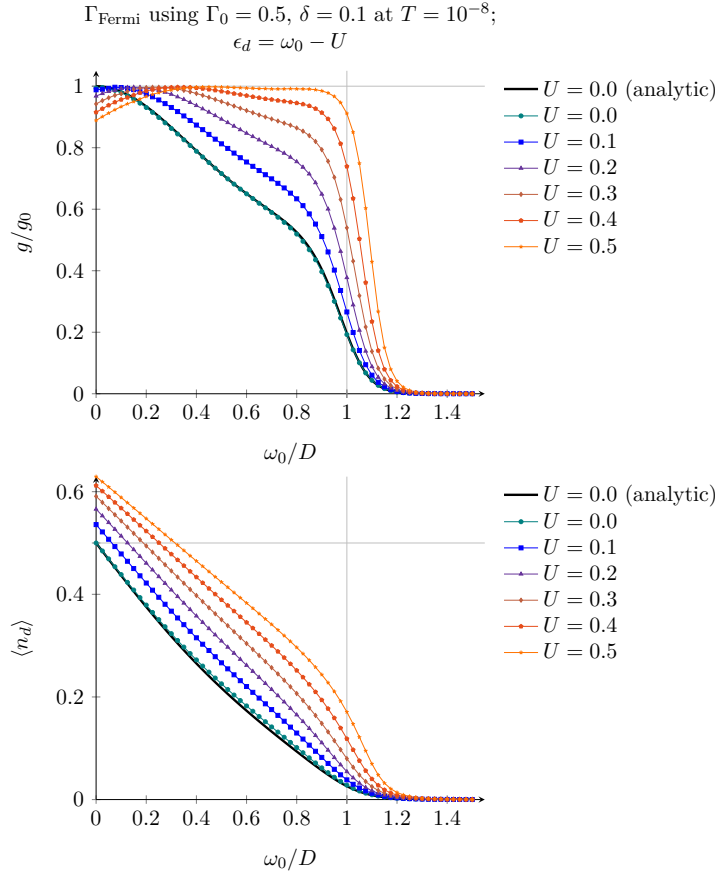


Figure 5.1: Conductance through the QPC and average occupation assuming a hybridization function shaped like a double-sided Fermi function for different values of the on-site interaction strength  $U$ . For high  $U = 0.5$ , the initial step in the conductance observed in experiments is reproduced very well. The shoulder apparent in this picture must not be confused with the 0.7-anomaly.

case, which has therefore no relation to the 0.7 anomaly. This explanation can be verified by scaling all parameters except the bandwidth by  $\frac{1}{2}$ , which corresponds to doubling the bandwidth.<sup>1</sup> This results in later onset of the cut-off, which confirms its dependence on the location of the band edge (see figure 5.2).

With increasing interaction strength, the conductance is enhanced. This can be explained by the observation that the spectral functions change their shape as the system is shifted. The peak of the spectral function becomes asymmetric for shifts  $\omega_0 > 0$  such that a greater portion of their weight is placed near the Fermi energy compared to the non-interacting case and the value of  $A(0)$  changes more slowly. This effect grows stronger as  $U$  is increased. Since a Fermi-shaped hybridization function is nearly constant within the band, the conductance stays near  $g_0$  until the band edge is reached. Thus, for  $U \approx 0.5$ , the first quantised step in the conductance from  $g = 0$  to  $g = g_0$  observed in experiments [1, 2, 18, 19] is reproduced. However, the 0.7 anomaly is not yet visible.

In the Kondo model, full conductance summed over spin gives the conductance  $g_0 = \frac{2e^2}{h}$ . Going to  $2g_0$  requires an additional transverse channel, which is beyond the current model. Therefore, instead of further increasing to  $g = 2g_0$  the conductance

<sup>1</sup>The former is accomplished more easily, as changing the value of  $D$  requires adjustment of NRG parameters.

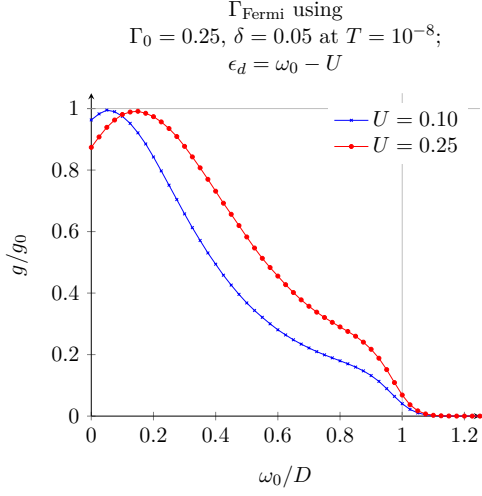


Figure 5.2: Scaling all parameters except the bandwidth  $D$  using a factor of  $\frac{1}{2}$  leads to later onset of the cutoff compared to the unscaled case in figure 5.1.

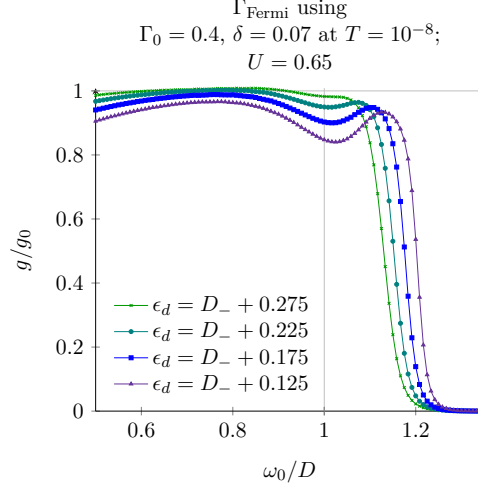


Figure 5.3: An impurity level close to the band edge makes sub-structures in the conductance curve appear. Their origin is the pinning of the spectral function to the Fermi edge.

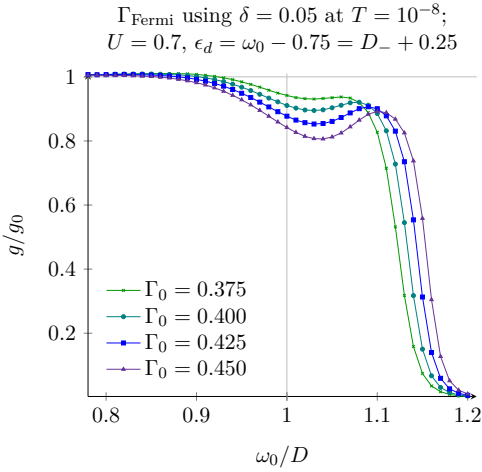


Figure 5.4: The strength of the sub-structure is directly related to the width of the spectral function, which is in turn controlled by hybridization strength.

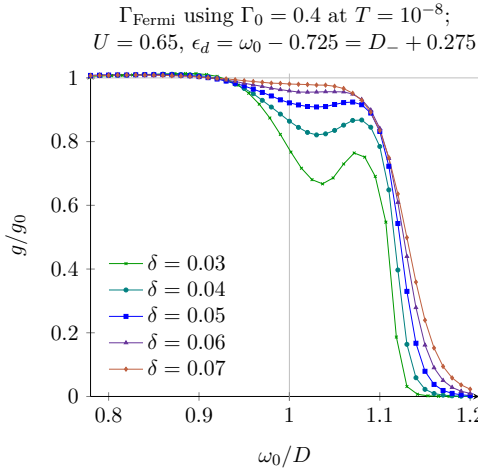


Figure 5.5: Broad band edges (large  $\delta$ ) make sub-structures disappear.

---

in this model drops for  $\omega_0 < 0$  due to the upper band edge.

The occupation number, also shown in figure 5.1, decreases almost linearly until the band edge is reached. Since the width of the spectral functions is similar to the bandwidth, the remaining weight below the Fermi energy is quickly lost at that point and the average occupation drops to zero.

When the impurity level is taken closer to the lower band edge, a peak appears beyond the band edge (see figure 5.3). The reason for this behaviour is again the change in shape of the spectral function, where always more weight is placed near the Fermi edge. This leads to an enhanced conductance in the range  $\omega_0 \approx 1.1$ . Further decrease of the distance between impurity level and lower band edge distorts the conductance step.

Additional evidence that this feature is caused by the band edge is the strong effect of variations in the hybridization strength  $\Gamma_0$  on the shape of the additional peak as shown in figure 5.4. Since the hybridization strength is roughly proportional to the width of the spectral function, a decrease in  $\Gamma_0$  decreases the weight of the spectral function near the band edge. Furthermore, smoother band edges (increased  $\delta$ ) directly lead to a smoothed structure, until it becomes invisible for large  $\delta$  (see figure 5.5).

While this feature initially seems similar to the 0.7 anomaly, results for a wide range of parameter sets exhibit qualitative differences to experimental observations. The data obtained from the SIAM using  $\Gamma_{\text{Fermi}}$  shows a shoulder at high conductance values of  $g/g_0 \gtrsim 0.9$  or a smaller peak with a significant drop in conductance between said peak and the plateau at  $g = g_0$ . In contrast, experimental data [1, 2, 12, 18] shows a sub-structure in the range of  $g/g_0 = 0.4$  to 0.9 in the shape of a shoulder or small step as opposed to a distinct peak.

## 5.4 Van Hove Ridges

For a hybridization function containing van Hove ridges, the resulting behaviour of the conductance for varied gate voltage does not match the experimentally observed behaviour very well (see figure 5.6). While an initial step from  $g = 0$  to  $g \approx g_0$  is visible for certain interaction strengths, the conductance drops again for further decrease of  $\omega_0$  and never forms the flat plateau near  $g_0$  which is observed in experiments (see [1, 2, 18, 19]). For interaction strengths  $U \gtrsim 0.2$ , the initial peak even exceeds  $g_0$ . This unphysical data occurs due to sensitivity of the conductance formula to inaccuracy in sampling the steep slope in the hybridization function near the band edges.

Further increase in  $U$  to  $\approx 0.5$  causes the peaks in hybridization strength and spectral function to cross  $\epsilon_F$  at distinct  $\omega_0$ , which is visible in the conductance as a split peak near the band edge. Thus, even though the decrease in conductance for shifts  $\omega_0 \approx 0.7$  shrinks for stronger on-site interactions, the peaks in the hybridization function and spectral function prevent a flat plateau. As an example,  $U = 0.8$  is shown in figure 5.6.

The simulated behaviour never resembles the experimental observations. For these reasons, the analysis of van Hove ridges in the hybridization function was not further pursued.

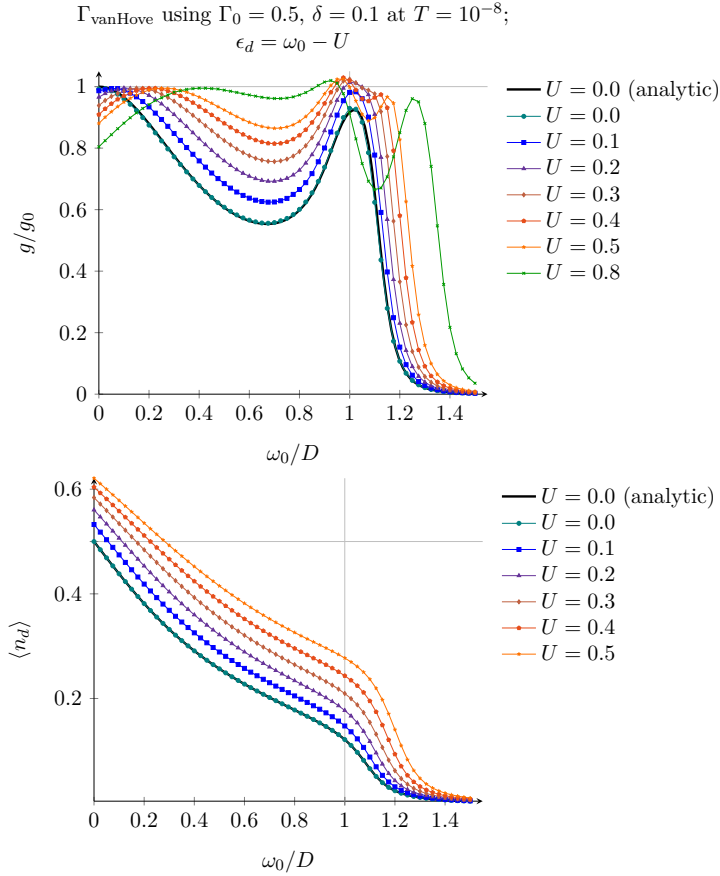


Figure 5.6: Conductance through the QPC and average occupation assuming a hybridization function with two peaks (van Hove ridges) at the band edges for different values of the on-site interaction strength  $U$ . Clearly, this hybridization function does not reproduce experimental results. The peaks where  $g$  exceeds  $g_0$ , which is unphysical behaviour, are due to inaccuracy in sampling near the van Hove singularities.

## 5.5 Semicircle

Increasing on-site interaction strength in the case of a semi-circular hybridization function cause a smooth transition to a broadened step function. This can be explained by the observation that for  $U > 0$ , the spectral functions become asymmetric in a similar way as in the case of a Fermi-shaped hybridization function. The resulting spectral functions (see figure 5.9) are now remarkably similar to the van Hove ridges proposed in the paper by Bauer et al. [1]. As has been pointed out in the derivation of the density of states of an infinite chain in section 2.3.3, this chain can be equivalently expressed as a single site coupled on two sites to a semi-infinite chain, which is a system with semi-circular spectral functions. This corresponds exactly to the situation in the QPC model and thus, the resemblance of the impurity spectral function to a van Hove singularity is to be expected.

The average occupation of the impurity state is very quickly cut off at the band edge after almost linear behaviour already familiar from the double-sided Fermi hybridization function. The sharper cut-off can be explained by the similarly sharper cut-off in the hybridization function as compared to the Fermi function.

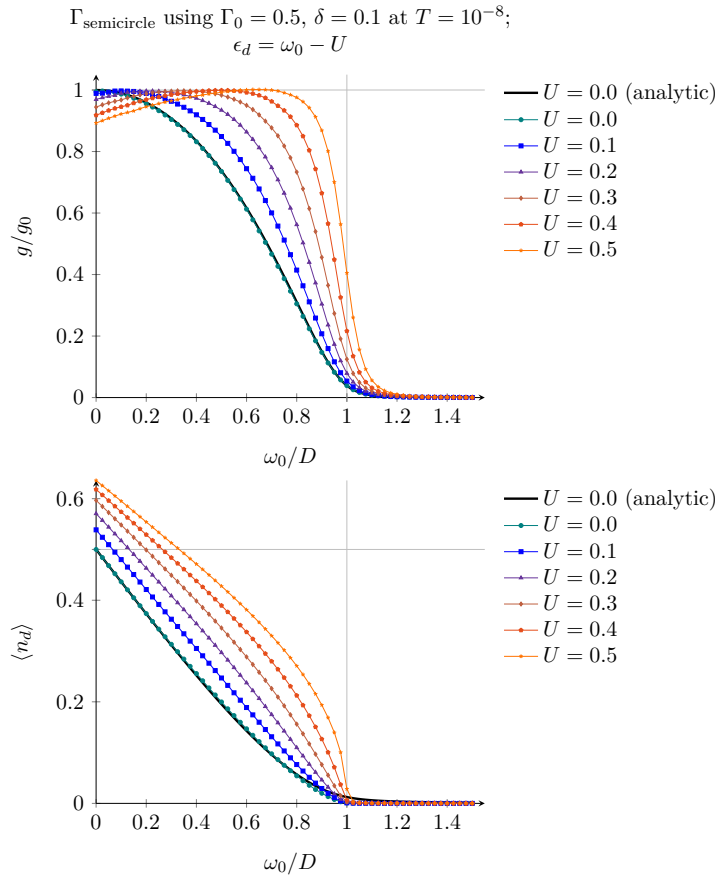


Figure 5.7: Conductance through the QPC and average occupation assuming a hybridization function of semi-circular shape for different values of the on-site interaction strength  $U$ . For a range of  $U$ , the initial step in the conductance observed in experiments is reproduced, similar to 5.1.

## 5.6 Anomaly in the Conductance Step

This section explores a sub-structures which can be found in the step structure of the conductance curve using the semi-circular hybridization function. Upon decreasing  $\delta$ , the band edge becomes sharper and some previously invisible features appear for large values of  $U \gtrsim \Gamma_0$ . For certain parameters, this feature develops a remarkable similarity to the 0.7 anomaly. Similar to the experimentally observed shape of the anomaly, a shoulder at a conductance  $g < g_0$  develops (see figure 5.8).

This feature shows several characteristic features of a Kondo-like effect, most notably a sharp peak in the spectral function at the Fermi energy (see figure 5.9). For small band shifts  $\omega_0$ , this peak is broadened by the hybridization  $\Gamma(\omega)$ ; only at the band edge, where  $\Gamma(\omega)$  drops to very low values, a very sharp peak centred on  $\epsilon_F$  develops, leading to high conductance in spite of low  $\Gamma(0)$ . As a consequence, the shape of this feature is very sensitive to small variations in  $\delta$ .

In contrast, further increase in on-site interaction energy  $U$  barely influences the behaviour. The reason for this is likely the fixed distance of  $\epsilon_d$  to the lower band edge, whereas only the upper level position  $\epsilon_d + U$  moves to even higher energies.

As discussed in section 2.6, the Kondo temperature indicates the order of magnitude of the dynamically generated lowest energy scale. The data shown in figure 5.8 shows that the location of the anomaly corresponds to a minimum in  $T_K$ , where a drop by one order of magnitude with respect to the value at the plateau occurs. This signifies enhanced spin susceptibility.

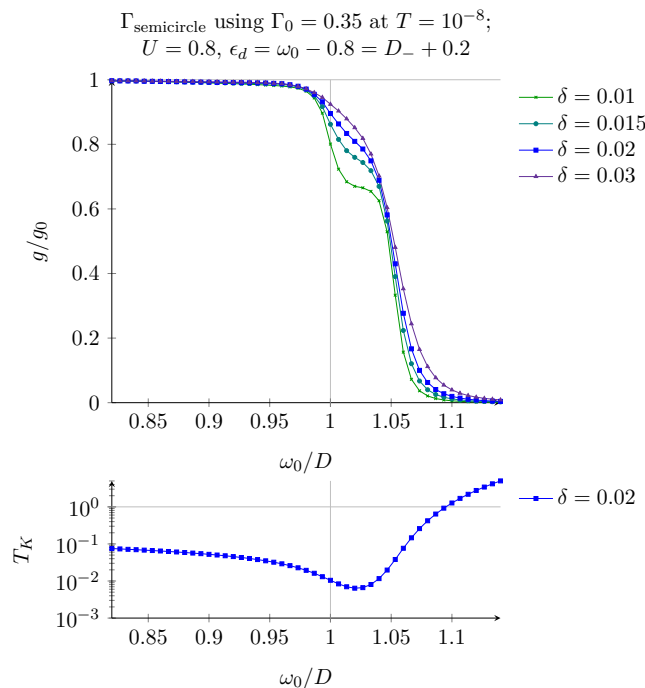


Figure 5.8: A structure which is very similar to the 0.7 anomaly. The Kondo temperature shows a minimum at the location of the anomaly, which corresponds to a maximum in spin susceptibility.

$\Gamma_{\text{semicircle}}$  using  $\Gamma_0 = 0.35$  and  $\delta = 0.02$  at  $T = 10^{-8}$   
 $U = 0.8, \epsilon_d = \omega_0 - 0.8 = D_- + 0.2$

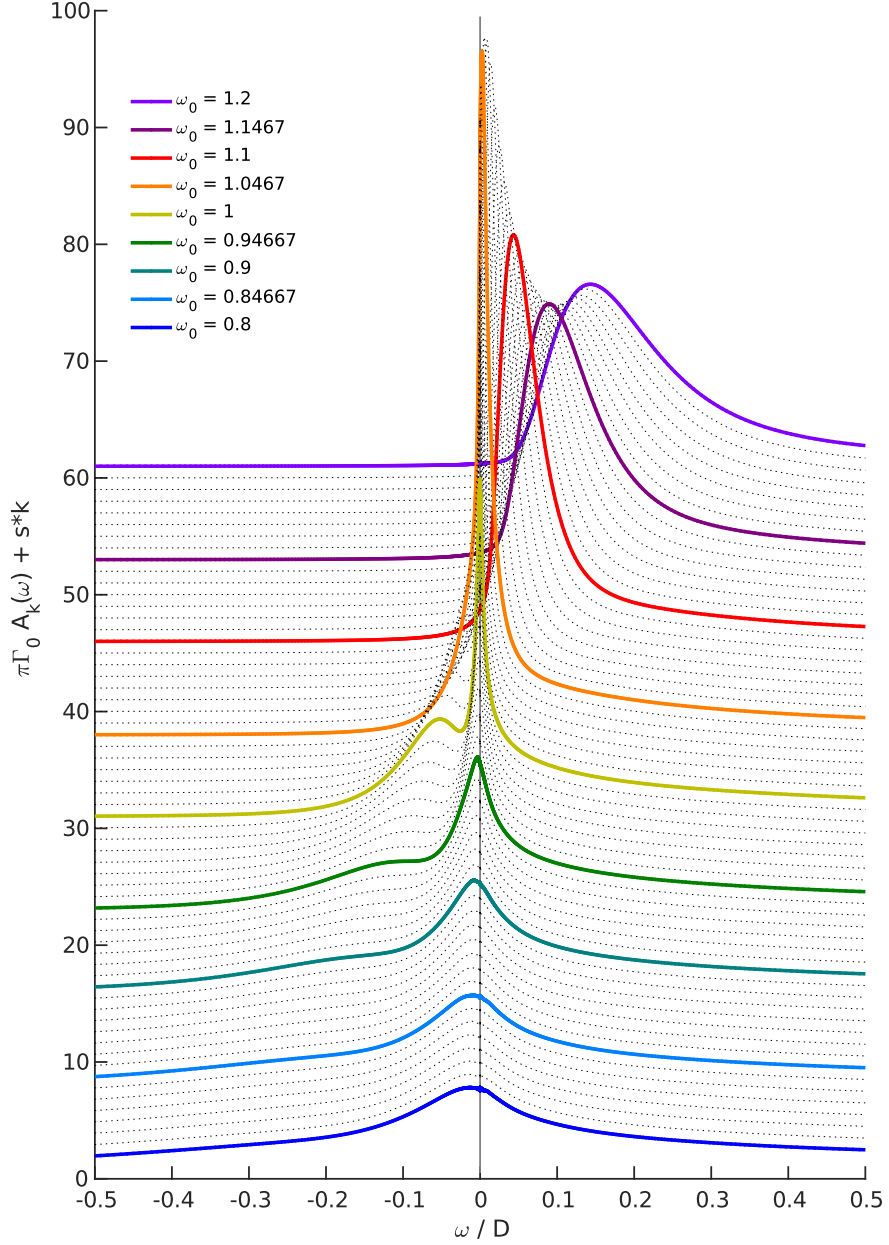


Figure 5.9: Spectral functions  $A_k(\omega)$  from which the conductances for  $\delta = 0.02$  in figure 5.8 were obtained. In the region of the 0.7 anomaly between  $\omega_0 = 1$  (lime) and  $\omega_0 \approx 1.05$  (orange), a very sharp Kondo peak occurs. The spectral functions  $A_k(\omega)$  were offset vertically by a constant  $s$  times  $k$  to create a pseudo-3d effect, such that  $\omega_0$  increases monotonically from bottom to top.

## 5.7 Finite Temperature

Results for finite temperature are shown in figure 5.10. As the minimal Kondo temperature is  $T_K \approx 10^{-2}$ , the shape of the anomaly remains the same for  $T \lesssim 10^{-4}$ . At higher temperatures comparable to the Kondo temperature, the peak in the spectral function is broadened by temperature and the lowest energy scale is determined by  $T$ .

At this point, the shoulder develops into a small peak. In the zero-temperature case, the superposition of the overall step structure and the small peak forms the anomaly. However, for higher temperatures, the peak structure unexpectedly turns out to be remarkably stable compared to the overall step structure including the plateau at  $g = g_0$ , which starts to decay at temperatures  $T \gtrsim 10^{-3} \approx 0.1 T_K$ . As a result, a peak separated from the plateau by a drop in conductance becomes visible.

In experiments, the falloff between plateau and 0.7 anomaly becomes broader with temperature as well [1, 2, 12, 18]. However, the conductance should eventually reach  $g_0$  at all temperatures, which is not reproduced by this model. The peak in conductance for high temperatures is not observed in experiments.

However, as previously mentioned, the behaviour of the system at  $\omega_0 \approx D$  shows high sensitivity to changes in  $\delta$ , which controls the weight of the hybridization function placed below the lower band edge. In this thesis, the weak hybridization to states below the band edge was modelled by convolution with a Lorentz peak. Since very little can be inferred about hybridization from experimental data, this choice is rather arbitrary. It is quite possible that a different choice may eventually result in better correspondence to experimentally observed behaviour for finite  $T$ .

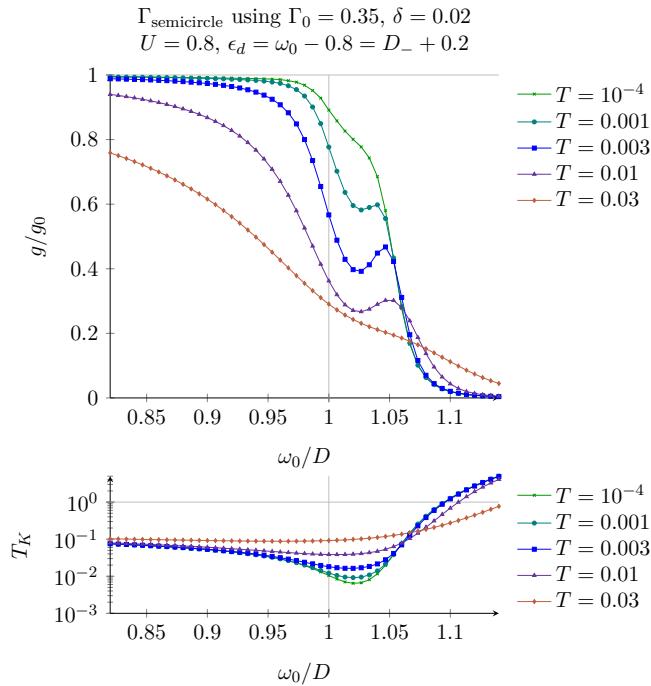


Figure 5.10: Behaviour of the anomaly for finite temperature. The smallest energy scale is never below  $\max(T, T_K)$ . There are some qualitative differences in the conductance compared to experimental results.

## Chapter 6

# Conclusion and Outlook

It has been shown that a single-impurity Anderson model can be solved accurately using the Open Wilson Chain approach to the NRG, even in the presence of a very structured hybridization function. The single-impurity Anderson model was used as a minimal model for a quantum point contact. Different hybridization functions were considered, and the behaviour of the model conductance at varied gate voltage compared to experimental observations. The quantised behaviour of conductance through a QPC is reproduced in the case of a hybridization function in the shape of a double-sided Fermi function or a semicircle, while a hybridization function with van Hove ridges leads to a number of deviations from experimentally observed behaviour. The latter was therefore not investigated further.

For the hybridization functions shaped like a double-sided Fermi function as well as the semi-circular hybridization function, a sub-structure in the conductance step is found. In the case of a semicircle, the sub-structure exhibits a shoulder with a shape similar to the experimentally observed 0.7 anomaly. Both the shape of the spectral function as well as the drop in Kondo temperature, which corresponds to enhanced spin susceptibility, indicate a Kondo-like effect. In the zero-temperature case, this model describes the anomaly quite well, while differences occur at finite temperature.

It is possible that these deviations from experimentally observed behaviour are caused by the particular shape of the hybridization function at the band edges. As the hybridization itself is not accessible in experiments, this choice is rather arbitrary. In this thesis, broadening was performed by convolution with a Lorentz peak. Choice of a different mollifier, for example one with exponential falloff, should have a strong effect on the shape of the anomaly and might result in behaviour which is closer to experimental observations.

Meanwhile, some open questions about the qualitative behaviour of the model remain. In particular, the dependence of the 0.7 anomaly on an external magnetic field  $B$  has been studied extensively [1, 2, 12, 18]. Calculations at finite  $B$  are possible within the NRG method as well. This would be the most obvious next step, which has not been performed in this work due to limitations in time. Furthermore, for finite- $B$  data to be sensible, it would be preferable to first achieve a better correspondence of the finite-temperature data to experimental observations.

# Acknowledgements

I am indebted to Andreas Weichselbaum, who always took the time to help me, to find intuitive and accessible explanations to my very frequent questions and also shared his code for the NRG. I am very grateful for his guidance during the work on my Bachelor's thesis.

I would like to thank Frauke Schwarz, Florian Stähler, Adriano di Pietro, Pol Alonso-Cuevillas Ferrer, Julian Thönni and Maximilian Kubullek for their helpful comments and suggestions. I would also like to thank the other members of the chair of theoretical solid state physics and Prof. Jan von Delft for allowing me to work on my Bachelor's thesis in a friendly and pleasant environment.

# Appendix

## A Kramers-Kronig Relations

The Kramers-Kronig relations are relations between the real and imaginary part of a complex function which is analytic in the upper half-plane.

Let  $f : \mathbb{C} \rightarrow \mathbb{C}$  be analytic in the upper half-plane  $\{z \mid \text{Im } z > 0\}$ . Then the following relations hold:

$$\text{Re } f(z) = \frac{1}{\pi} \mathcal{P} \int_{-\infty}^{\infty} dw \frac{\text{Im } f(w)}{w - z} \quad (\text{A.1})$$

$$\text{Im } f(z) = -\frac{1}{\pi} \mathcal{P} \int_{-\infty}^{\infty} dw \frac{\text{Re } f(w)}{w - z} \quad (\text{A.2})$$

where  $\mathcal{P}$  denotes the Cauchy principal value [13]. In this thesis, the principal value was obtained using

$$\mathcal{P} \int_{-\infty}^{\infty} dw \frac{\dots}{w - z} = \text{Re} \lim_{\eta \rightarrow 0} \int_{-\infty}^{\infty} dw \frac{\dots}{w + i\eta - z} = \int_{-\infty}^{\infty} dw \frac{\dots}{w^+ - z} \quad (\text{A.3})$$

where the last expression is merely a convenient shorthand.

## B Retarded Green's Functions

The retarded Green's function for two fermionic operators  $A, B$  is defined as [4]

$$i G_{A,B}^R(t, t') = \theta(t - t') \langle \{A(t), B(t')\} \rangle \quad (\text{B.1})$$

where the expectation value  $\langle \cdot \rangle$  is to be taken in respect to a thermal density matrix  $\rho$ . If the Hamiltonian is not time-dependent, the Green's function will only depend on  $t - t'$ . In this case, the Green's function becomes

$$i G_{A,B}^R(t) = \theta(t) \langle \{A(t), B(0)\} \rangle \quad (\text{B.2})$$

Taking the time derivative and using the Heisenberg equation of motion yields the equation of motion for the Green's function:

$$\begin{aligned} i \frac{d}{dt} G_{A,B}^R(t) &= \delta(t) \langle \{A(0), B(0)\} \rangle - i \theta(t) \langle \{[A, H](t), B(0)\} \rangle \\ &= \delta(t) \langle \{A(0), B(0)\} \rangle + G_{[A,H],B}^R(t) \end{aligned} \quad (\text{B.3})$$

This equation can be Fourier-transformed to its frequency-space version:

$$\omega^+ G_{A,B}^R(\omega) = \langle \{A(0), B(0)\} \rangle + G_{[A,H],B}^R(\omega) \quad (\text{B.4})$$

This equation is particularly useful for many calculations.

Retarded Green's functions can be used to calculate different quantities, most notably the *spectral function*. The spectral function of a state  $c^\dagger$  is given by [6, 11]

$$A_c(\omega) = -\frac{1}{\pi} \text{Im} G_{c,c^\dagger}^R(\omega) \quad (\text{B.5})$$

# Bibliography

- [1] Florian Bauer et al. ‘Microscopic origin of the ‘0.7-anomaly’ in quantum point contacts’. In: *Nature* 501 (Sept. 2013), pp. 73–78. DOI: 10.1038/nature12421.
- [2] B. Brun et al. ‘Electron Phase Shift at the Zero-Bias Anomaly of Quantum Point Contacts’. In: *Phys. Rev. Lett.* 116.13 (Mar. 2016), p. 136801. DOI: 10.1103/PhysRevLett.116.136801.
- [3] B. Bruognolo et al. ‘Open Wilson chains for quantum impurity models: Keeping track of all bath modes’. In: *Phys. Rev. B* 95.12 (Mar. 2017), p. 121115. DOI: 10.1103/PhysRevB.95.121115.
- [4] Henrik Bruus and Karsten Flensberg. *Many-Body Quantum Theory in Condensed Matter Physics. An introduction*. Oxford University Press, 2009. ISBN: 978-0-19-856633-5.
- [5] Ralf Bulla, Theo A. Costi and Thomas Pruschke. ‘Numerical renormalization group method for quantum impurity systems’. In: *Rev. Mod. Phys.* 80.2 (Apr. 2008), pp. 395–450. DOI: 10.1103/RevModPhys.80.395.
- [6] Piers Coleman. *Introduction to Many-Body Physics*. Cambridge: Cambridge University Press, 2015. ISBN: 978-0-521-86488-6.
- [7] T. A. Costi, A. C. Hewson and V. Zlatic. ‘Transport coefficients of the Anderson model via the numerical renormalization group’. In: *Journal of Physics: Condensed Matter* 6.13 (1994), p. 2519. DOI: 10.1088/0953-8984/6/13/013.
- [8] Elbio Dagotto. ‘Correlated electrons in high-temperature superconductors’. In: *Rev. Mod. Phys.* 66.3 (July 1994), pp. 763–840. DOI: 10.1103/RevModPhys.66.763.
- [9] Alexander L. Fetter and John Dirk Walecka. *Quantum Theory of Many-Particle Systems*. Dover Publications, 2003. ISBN: 978-0-486-42827-7.
- [10] H. O. Frota and L. N. Oliveira. ‘Photoemission spectroscopy for the spin-degenerate Anderson model’. In: *Phys. Rev. B* 33.11 (June 1986), pp. 7871–7874. DOI: 10.1103/PhysRevB.33.7871.
- [11] Alexander Cyril Hewson. *The Kondo Problem to Heavy Fermions*. Cambridge studies in magnetism. Cambridge: Cambridge University Press, 1993. ISBN: 978-0-521-59947-4.
- [12] Jan Heyder et al. ‘Relation between the 0.7 anomaly and the Kondo effect: Geometric crossover between a quantum point contact and a quantum dot’. In: *Phys. Rev. B* 92.19 (Nov. 2015), p. 195401. DOI: 10.1103/PhysRevB.92.195401.
- [13] John David Jackson. *Classical Electrodynamics*. New York: Wiley, 2001. ISBN: 0-471-30932-X.

- [14] H. R. Krishna-murthy, J. W. Wilkins and K. G. Wilson. ‘Renormalization-group approach to the Anderson model of dilute magnetic alloys. I. Static properties for the symmetric case’. In: *Phys. Rev. B* 21.3 (Feb. 1980), pp. 1003–1043. DOI: 10.1103/PhysRevB.21.1003.
- [15] David C. Langreth. ‘Friedel Sum Rule for Anderson’s Model of Localized Impurity States’. In: *Phys. Rev.* 150.2 (Oct. 1966), pp. 516–518. DOI: 10.1103/PhysRev.150.516.
- [16] Yigal Meir, Kenji Hirose and Ned S. Wingreen. ‘Kondo Model for the “0.7 Anomaly” in Transport through a Quantum Point Contact’. In: *Phys. Rev. Lett.* 89.19 (Oct. 2002), p. 196802. DOI: 10.1103/PhysRevLett.89.196802.
- [17] Yigal Meir and Ned S. Wingreen. ‘Landauer formula for the current through an interacting electron region’. In: *Phys. Rev. Lett.* 68.16 (Apr. 1992), pp. 2512–2515. DOI: 10.1103/PhysRevLett.68.2512.
- [18] K. J. Thomas et al. ‘Possible Spin Polarization in a One-Dimensional Electron Gas’. In: *Phys. Rev. Lett.* 77.1 (July 1996), pp. 135–138. DOI: 10.1103/PhysRevLett.77.135.
- [19] B. J. van Wees et al. ‘Quantized Conductance of Point Contacts in a Two-Dimensional Electron Gas’. In: *Phys. Rev. Lett.* 60.9 (Feb. 1988), pp. 848–850. DOI: 10.1103/PhysRevLett.60.848.
- [20] Andreas Weichselbaum. ‘Discarded weight and entanglement spectra in the numerical renormalization group’. In: *Phys. Rev. B* 84.12 (Sept. 2011), p. 125130. DOI: 10.1103/PhysRevB.84.125130.
- [21] Andreas Weichselbaum. ‘Tensor networks and the numerical renormalization group’. In: *Phys. Rev. B* 86.24 (Dec. 2012), p. 245124. DOI: 10.1103/PhysRevB.86.245124.
- [22] Kenneth G. Wilson. ‘Renormalization group methods’. In: *Advances in Mathematics* 16.2 (1975), pp. 170–186. ISSN: 0001-8708. DOI: [http://dx.doi.org/10.1016/0001-8708\(75\)90149-8](http://dx.doi.org/10.1016/0001-8708(75)90149-8).
- [23] Kenneth G. Wilson. ‘The renormalization group: Critical phenomena and the Kondo problem’. In: *Rev. Mod. Phys.* 47.4 (Oct. 1975), pp. 773–840. DOI: 10.1103/RevModPhys.47.773.
- [24] M. Yoshida, M. A. Whitaker and L. N. Oliveira. ‘Renormalization-group calculation of excitation properties for impurity models’. In: *Phys. Rev. B* 41.13 (May 1990), pp. 9403–9414. DOI: 10.1103/PhysRevB.41.9403.

---

Hiermit erkläre ich, die vorliegende Arbeit selbständig verfasst und keine anderen als die angegebenen Quellen und Hilfsmittel benutzt zu haben.

München, 24. Juli 2017

Marc Ritter